Article

Electrokinetically Forced Turbulence in Microfluidic Flow

Willy L. Duffle [1] and Evan C. Lemley [2,*]

[1] University of Central Oklahoma; wduffle@uco.edu
[2] University of Central Oklahoma; elemley@uco.edu
* Correspondence: elemley@uco.edu; Tel.: +01-405-974-5473

Abstract: While laminar flow heat transfer and mixing in microfluidic geometries has been investigated experimentally, as has the effect of geometry-induced turbulence in microfluidic flow (it is well documented that turbulence increases convective heat transfer in *macro*fluidic flow), little literature exists investigating the effect of electrokinetically-induced turbulence on heat transfer at the micro scale. Using recently observed experimental data, this work employed computational fluid dynamics coupled with electromagnetic simulations to determine if electrokinetically-forced, low-Reynolds number turbulence could be observed in a rectangular microchannel with using Newtonian fluids. Analysis of the results was done via comparison to the experimental criteria defined for turbulent flow. This work shows that, even with a simplified simulation setup, computational fluid dynamics (CFD) software can produce results comparable to experimental observations of low-Reynolds turbulence in microchannels using Newtonian fluids. In addition to comparing simulated velocities and turbulent energies to experimental data this work also presents initial data on the effects of electrokinetic forcing on microfluidic flow based on entropy generation rates.

Keywords: micro-fluidics, micro-mixer, entropy generation, micro-turbulence, electrokinetic mixer

1. Introduction

Fluid flow in microscale devices (microfluidics) has become an important area to study for applications in recent years. With an expanding set of techniques to create microchannels of increasingly complex geometries and recent biomedical and security applications, the interest in microfluidics continues to increase. Two important applications are micro-mixing and micro heat exchangers. The difficulty in mixing and heating fluids at the microscale is that the fluid flow is almost always laminar. The chaotic nature of turbulent flow at the macroscale is useful for both mixing and heating, but is an unusual phenomenon at the microscale. Many efforts have been made to create chaotic advection in microscale applications [1], which in some sense can mimic turbulence.

Although turbulence in the laminar flow of Newtonian fluids at the microscale is an unusual occurrence, some recent experimental reports have claimed turbulent behavior at Reynolds numbers far below typical accepted values [2].

Computational fluid dynamics (CFD) simulations can provide a benefit to researchers as a tool to either design experiments or improve validation of experiments. Simulations require benchmarks to validate their results and these benchmarks may be numerical or experimental in nature.

Previous efforts to validate laminar microscale flow with CFD have been successful. Unlike *Passive mixing*, which uses the geometry of microchannels to increase mixing efficiency, *Active mixing* uses external forces such as acoustically driven vibration [3] or external electric and magnetic fields [4,5] to force mixing. Attempts to model active mixing applications are ongoing, but researchers often choose to perform experiments because of the complexities involved in the modeling of these microscale phenomena. An additional level of complexity to add to the modeling of these active

Preprints (www.preprints.org) | NOT PEER-REVIEWED | Posted: 19 November 2018 doi:10.20944/preprints201811.0462.v1

mixers would be to include the existence of low Reynolds number, electrokinetically-induced turbulence, or μEKT [6].

The objectives of this work were:

- To determine the feasibility of observing turbulence in an electrokinetically-forced microfluidic mixer using CFD.
- To quantify the effects of electrokinetic forcing in microfluidic mixing using CFD.
- To quantify the entropy generation in an electrokinetically-forced microfluidic mixer using CFD.

2. Methodology

To build the simulation model based on the Wang et al. experiments it first had to be determined how to model the force due to the applied electric field. The model used the laminar flow equations of Navier-Stokes with a body force, $\vec{F}_e$, included (see Equation 1).

$$\rho \frac{D\vec{v}}{Dt} = -\nabla P + \mu \nabla^2 \vec{v} + \vec{F}_e, \tag{1}$$

Wang et al. defined this force as

$$\overrightarrow{F_e} = \rho_f \vec{E} - \frac{1}{2}(\vec{E} \cdot \vec{E})\nabla\varepsilon + \frac{1}{2}\left[\rho \vec{E} \cdot \vec{E}\left(\frac{\partial \varepsilon}{\partial \rho}\right)\right]_T, \tag{2a}$$

The RHS terms represent the contributions due to the Coulomb force, the dielectric force and the force due to thermal expansion, respectively. ε is the fluid permittivity, and ρ is the fluid density [6,7] and ρ_f represents the free charge density:

$$\rho_f = -\frac{\varepsilon \vec{E} \cdot \vec{\nabla}\sigma}{\sigma}, \tag{2b}$$

The partial derivative in Equation (2a) disappears for an incompressible fluid and the second term is negligible compared to the first when dealing with fluids of different conductivities [6], the following simplification can be made for the electric body force

$$\overrightarrow{F_e} = \rho_f \vec{E}, \tag{3}$$

2.1 The Model

The simulation model was built using SolidWorks® 3D design software for the modeling of the physical geometry and COMSOL Multiphysics® for the computational modeling. The bulk of the CFD runs utilized the University of Central Oklahoma's (UCO) BUDDY supercomputer cluster. BUDDY is a 38-node Linux cluster with one control node, 31 compute nodes (20 CPUs with 64GB total memory), 4 high memory compute nodes (20 CPUs with 128GB total memory) and 2 GPU nodes.

The initial conditions for this work were taken from the experimental conditions [2,6]. The side walls of the microchannel were defined as gold foil with all other walls being acrylic. The fluids defined were de-ionized water and a phosphate buffer solution though this work used a saline solution instead of phosphate; the important factors in choosing a working fluid was to ensure it was Newtonian and that the electrical conductivity gradient was 5000:1. The AC electric field range investigated was 0-20V_{pp} with a phase difference between electrodes of 180 degrees. This potential was defined as a DC voltage on the electrodes.

The geometry was split into two fluid domains. At time t = 0s the two fluids are completely unmixed resulting in a virtual boundary along the centreline of the microchannel (see Figure 1) with a conductivity gradient of 5000:1. At the point where the two fluids meet the concentration gradient remains at a maximum while the downstream concentration gradient moves toward equilibrium.

Preprints (www.preprints.org) | NOT PEER-REVIEWED | Posted: 19 November 2018 doi:10.20944/preprints201811.0462.v1

Because the electrodes are non-parallel, they are closest at the entrance creating a maximum electric field value there [2] and from Equation 3 it can be seen that the greatest electric field yields the greatest body force.

The inlet geometry was designed for the model to ensure laminar flow at the channel entrance and the channel length was approx. 5mm. The flow parameters shown in **Table** were used to match the inputs to the physical experiments by Wang et al. The calculated outputs provided a reference for the values expected if the simulations were valid.

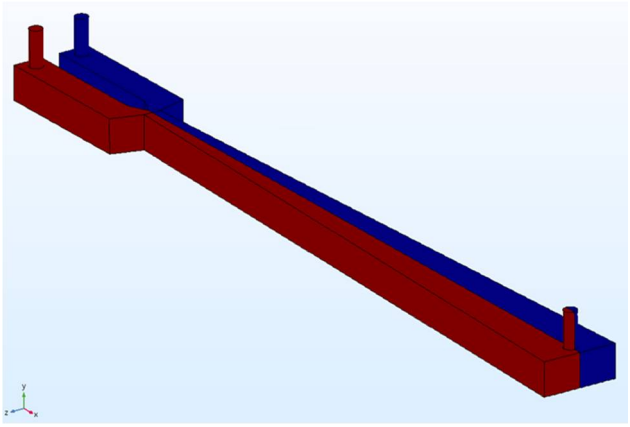

Figure 1. Two fluid domains considered in this work.

2.2 Simulation Software

COMSOL Multiphysics® couples multiple physics interfaces together automatically but also allows the user the manually couple if needed. This work makes use of the *Electric Currents*, *Laminar Flow* and *Transport of Diluted Species (TDS)* interfaces with the *Electric Currents & Laminar Flow* automatically coupled while the *Laminar Flow* and *Transport of Diluted Species* were manually coupled.

Because the problem to be solved was complex, simplifications were required. The primary

Table 1. Initial and Boundary Conditions (20Vpp shown)

	Voltage Potential (V)	Velocity (m/s)	Pressure (Pa)	Flowrate (m^3/s)	Body Force - i^{th} component (N/m^3)	NaCl Concentration (mol/m^3)
Electric Current (Positive Electrode)	10				$\rho_f * E_i$	
Electric Current (Negative Electrode)	-10				$\rho_f * E_i$	
Laminar Flow (at each inlet)		0.0042				
Pressure (at outlet)			0	6.66E-11		
Initial Conditions (internal)	0	0	0	0		
Transport of Diluted Species						2.88
Species Flux (at each inlet)		υ				2.88 * υ

simplification was to disable the *migration in an electric field* option in the TDS interface; while this interaction would exist in any physical experiment, this work was trying to quantify the *specific* effects due to enhanced mixing caused by μEKT which would justify ignoring effects that would be present if an electric field was applied but μEKT was absent. To justify this omission, two assumptions were made: 1) the migration due *solely* to the electric field acting on the charged species would be the same with or without turbulence and 2) the fluid-particle interaction is negligible meaning the additional

Preprints (www.preprints.org) | NOT PEER-REVIEWED | Posted: 19 November 2018 doi:10.20944/preprints201811.0462.v1

particle motion would not appreciably effect the flow, together these assumptions render the migration inconsequential when comparing total entropies between forced and unforced cases.

For the second assumption, the Stokes drag coefficient

$$C_D = \frac{2F_d}{\rho v^2 A} = \frac{24}{Re}, \quad (4)$$

can be manipulated to find the drag force

$$\vec{F}_d = 3\pi\mu\vec{v}D_{eff}, \quad (5)$$

created by the Na^+ and Cl^- ions moving through the solution in the electric field, a force which was found to be negligible compared to the electric body force (F_d ~ 10^{-7} N vs F_e ~ 10^5 N).

In addition, the particle diameters were small enough that the electrophoretic force was deemed negligible as well, on the order of 10^{-27} N.

Figure 2 shows the relationship between the physics interfaces after the problem was simplified. Comsol automatically uses steady state solution steps as the initial conditions for a transient study step when applicable to prevent mismatched boundary conditions at t = 0. The electric field was solved as a steady state DC potential on the electrodes and then the electric field components were multiplied by $\cos(\omega t)$ to calculate the electric body force components used as the driving force in Navier-Stokes, seen in Equation 1. The force is defined in COMSOL as a Volume force and it was added into the *Laminar Flow* interface as shown in Figure 3.

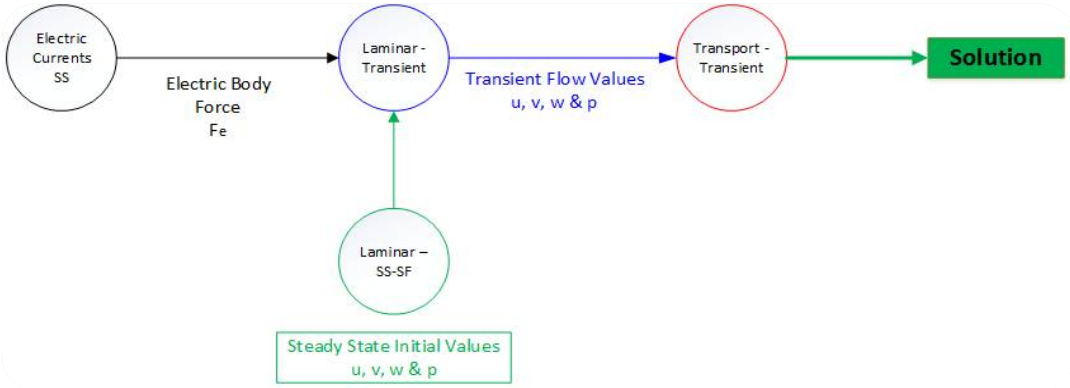

Figure 2. Governing physics setup for simulations.

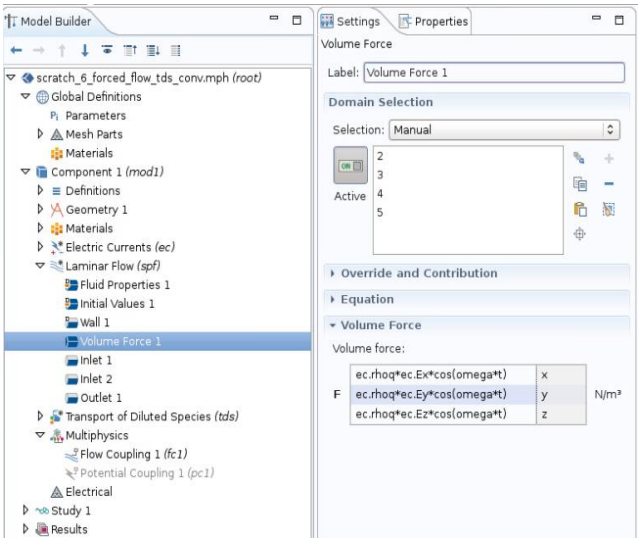

Preprints (www.preprints.org) | NOT PEER-REVIEWED | Posted: 19 November 2018 doi:10.20944/preprints201811.0462.v1

Figure 3. Implementation of Volume Force in COMSOL.

The stationary study steps in the final simulation runs were done using an iterative, segregated solver while the time dependent solver for the *Laminar Flow* step was done using a fully-coupled, iterative solver and the solver for the *Transport of Diluted Species* was a fully-coupled, direct solver (MUMPS). The iterative method uses the Newton-Raphson method and the difference between segregated and fully-coupled approaches is how the equations for the different physics interfaces are related. The *Transport of Diluted Species* elements were cubic and the *Electric Currents* elements were quadratic. The fluid discretization setting for the *Laminar Flow* interface was set to **P2 + P1**; this setting denotes second order elements for the velocity components and linear elements for the pressure field.

2.3 Entropy

Why study the entropy of a system? When comparing two different physical processes it is first necessary to find a common relationship between them to base the comparison on. For example, when measuring the effectiveness of a heat transfer process, it is accepted practice to look at the Nusselt number Nu as a performance gauge [8]. For internal flow one looks at the pressure differential to determine system losses, which is good for comparing the efficiency of a design as it relates to frictional flow loss. However, if the system involves heat transfer as well, the temperature differential is used to quantify thermal losses. Pressure drop is measured in Pascals while temperature gradients are measured in degrees (Kelvin, Celsius or Fahrenheit), two units that do not add together for the purpose of determining a total system loss without first converting to some unit-less expression.

To describe the total system loss requires all involved expressions to be comparable in terms of units and order which is where the study of entropy really starts to make sense. Entropy ([W/K·m^3]) can be calculated from the incompatible variables of each process (fluid flow, heat transfer, species diffusion etc.), typically in post processing, when using finite element software. Once a single equation of similar terms is expressed, cause-effect relationships can be more readily seen. Adding the entropy equations for each of these individual physics processes together gives an equation for the total entropy generation for the system. Because isothermal conditions are assumed throughout the simulation, Equation 6 contains only a viscous dissipation term for laminar flow (in brackets) and a term to cover the entropy generated by diffusion of species.

$$S'''_{gen} = \frac{\mu}{T}\left\{ \begin{array}{c} 2\left[\left(\frac{\partial u}{\partial x}\right)^2 + \left(\frac{\partial v}{\partial y}\right)^2 + \left(\frac{\partial w}{\partial z}\right)^2\right] \\ + \left(\frac{\partial u}{\partial y} + \frac{\partial v}{\partial x}\right)^2 + \left(\frac{\partial u}{\partial z} + \frac{\partial w}{\partial x}\right)^2 + \left(\frac{\partial v}{\partial z} + \frac{\partial w}{\partial y}\right)^2 \end{array} \right\} + \frac{RD}{C}\left[\left(\frac{\partial C}{\partial x}\right)^2 + \left(\frac{\partial C}{\partial y}\right)^2 + \left(\frac{\partial C}{\partial z}\right)^2\right] \geq \emptyset \ , \qquad (6)$$

2.4 Mesh Study

To get accurate results in a finite element analysis, a mesh convergence study can be used to determine the optimal mesh size needed to balance the computational cost with the desired solution accuracy. A laminar flow simulation was completed for 4 meshes of increasing resolution (Coarser, Coarse, Normal and Fine) at a forcing voltage of 20V_{pp}. In this case many of the parameters of interest are derived from velocity but with both positive and negative velocity values it was difficult to compare volumetric totals.

The mesh study looked at the total values for T_e and S_{gen} over the volume shown in Figure 4 at each mesh size. Because the differences were on the order of 10^{-11} for each mesh, it shows that the choice of mesh in this case is arbitrary as the velocities involved are on the order of 10^{-3}, the values of T_e are on the order of 10^{-6} with S_{gen} at the channel entrance are as high as 200.

Preprints (www.preprints.org) | NOT PEER-REVIEWED | Posted: 19 November 2018 doi:10.20944/preprints201811.0462.v1

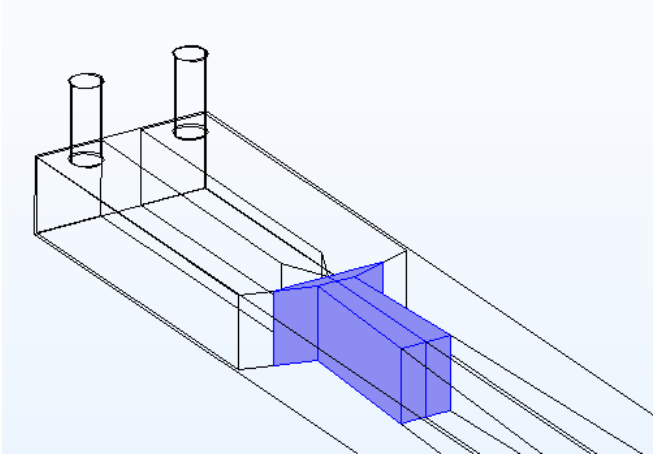

Figure 4. Volume from trailing edge to x = 0.5mm.

For this reason the Coarse Mesh, shown in **Error! Reference source not found.**, was used as it was the best choice in regard to solution time with each voltage run taking approximately 1hr 22min with *Transport of Diluted Species* included. For comparison, *without* TDS, a simple forced flow simulation with a *Normal* mesh resolution took 1hr 47min and the *Fine* resolution took 2hrs 33min.

The elements making up the meshes included tetrahedral, pyramid, prism, triangular, quadrilateral, edge and vertex elements.

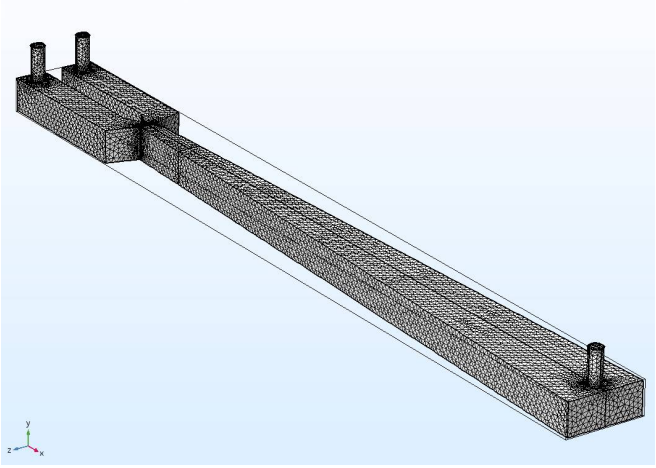

Figure 5. Course mesh used in mesh resolution study.

3. Results

The results reported are for simulation runs conducted over a period of 0.25s, over the voltage range of 0-20V_{pp}, with the values of interest examined in the volume of fluid from the point where the streams converge to the plane x = 0.5mm (shown in Figure 4). All the figures presented here are at t = 0.25s.

In Wang et al., the experimental results are discussed as they relate to six indicators of turbulent flow[2]: fast diffusion, high dissipation, irregularity, multi-scale eddies, continuity and 3-D flow. Of these six parameters, this work presents results correlating to four: high dissipation, fast diffusion, 3-D flow and irregularity.

 doi:10.20944/preprints201811.0462.v1

3.1 Fast Diffusion

From Figure 5 it can be seen that, without forcing, the flow is completely laminar and becomes more turbulent in appearance as the forcing voltage increases. While comparing the simulation stream lines to the LIFPA images of diffusion in the Wang experiment is not completely analogous, the experiment's visualization images using polystyrene particles as tracing devices shows similar results to the streamlines in **Error! Reference source not found.**.

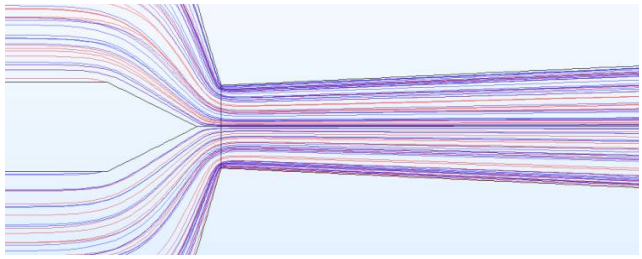

Figure 5. Streamlines - 0Vpp (Unforced).

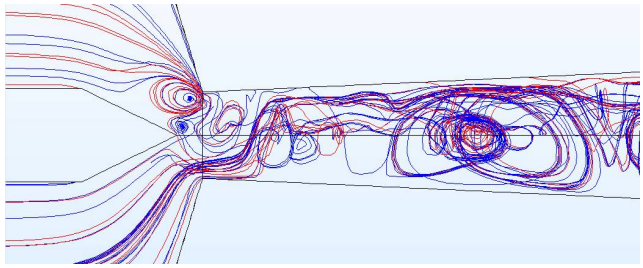

Figure 6. Streamlines - 20Vpp.

The effect of the electric field on dissipation can be seen in Figure 7 & Figure 8 with slices shown at x = 0, 100, 200, 300, 400, & 500μm. At a forcing voltage of $20V_{pp}$ the mixture appears to be completely homogenous at the plane x = 0.5mm. Because the two fluid domains are discretely populated at t = 0s with fluids of concentrations shown in the inlets, Figure 8 shows that homogeneity disappears shortly after this plane but it can be assumed that if the simulation was continued past 0.25s, the entire channel would become completely mixed due to the developing secondary flows that can be clearly seen downstream.

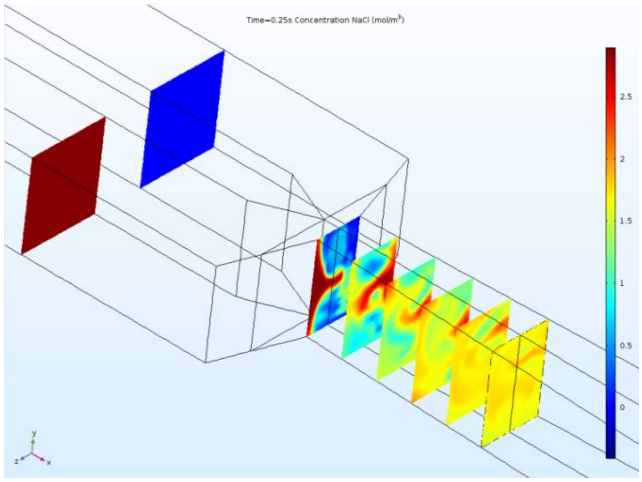

Figure 7. NaCl concentration (mol/m3) @ 20Vpp, t=0.25s (Slices at 100μm intervals).

Preprints (www.preprints.org) | NOT PEER-REVIEWED | Posted: 19 November 2018 doi:10.20944/preprints201811.0462.v1

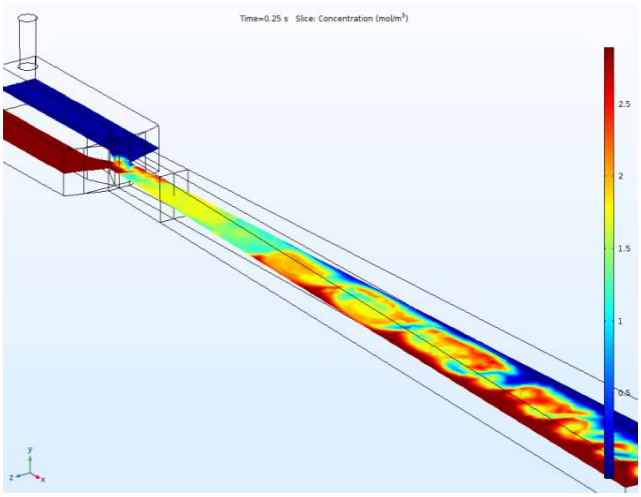

Figure 8. Downstream NaCl concentration (mol/m3) @ 20Vpp, t=0.25s.

3.2 High Dissipation

In macro-flows, a rapid, non-linear increase in the turbulent dissipation (another way of denoting pressure drop) signals the release of turbulent energy [2] so if the dissipation rate is high then the rate of change of turbulent energy is also high, indicating turbulence. The turbulent energy, T_e, was calculated at the point (100, 0, 0). When using turbulent models, one of the dependent variables calculated by COMSOL is the turbulent energy (T_e), however, because the simulations were completed using a *Laminar Flow* study instead of *Turbulent Flow* study, an equation was created to derive the value of T_e from laminar flow data starting from the definition [2]

$$T_e = \langle u_s'^2 \rangle, \quad (7)$$

where

$$u_s' = u_s - \langle u_s \rangle, \quad (8)$$

and given that, in 3-dimensions,

$$u_s = \sqrt{u^2 + v^2 + w^2}, \quad (9)$$

the equation used in COMSOL for post-processing (given 25 time steps) was

$$T_e = sum(\ (us - (sum(us, t, 0, t\_end)/25))\ \hat{}2, t, 0, t\_end\ )/25, \quad (10)$$

The Electric Rayleigh number was defined as [2]

$$Ra_e = \frac{\varepsilon w^2 E_0^2 (\sigma_2 - \sigma_1)}{\sigma_1 \mu\, D_e}, \quad (11)$$

And in COMSOL for each electrode potential difference was

$$Ra_e = ((80.2 * root.epsilon0\_const) * (2 * (V0\hat{}2)) * (0.0275 - 5.56e - 6))/(5.5e - 6 * 0.001[Pa * s] * 1.5e - 9[m\hat{}2/s]), \quad (12)$$

When T_e is plotted vs. Ra_e, as shown in Figure 9 & Figure 10, the rapid increase in turbulent energy after reaching the critical Rayleigh number [2] can be seen. A voltage range of 2-20V_{pp} was used for the data set and the plots, when compared, show a similar trend, electric Rayleigh number

 doi:10.20944/preprints201811.0462.v1

and range (within the same order of magnitude).

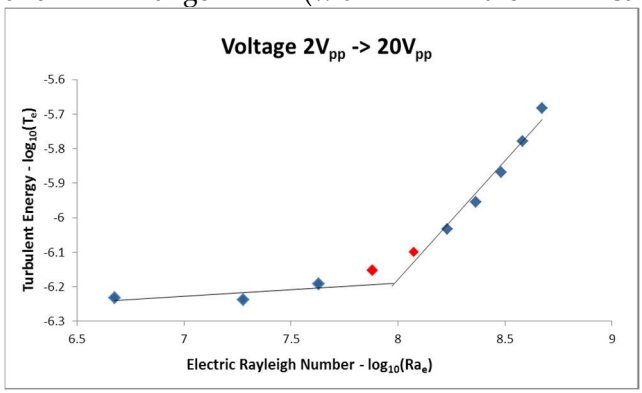

Figure **9.** *Te* vs *Rae* (from simulated data).

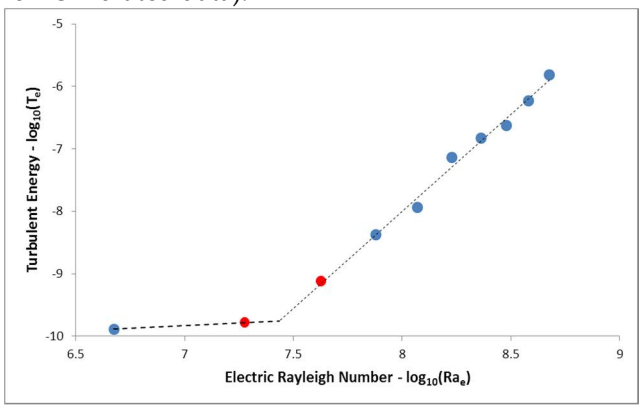

Figure 10. *Te* vs *Rae* (from experimental data).

Preprints (www.preprints.org) | NOT PEER-REVIEWED | Posted: 19 November 2018 doi:10.20944/preprints201811.0462.v1

Table 1 clearly shows that while the slopes are smaller than the experimental values by one order of magnitude, the relationship between the turbulent and laminar slopes (how much greater the turbulent slope is than the laminar) is closer in value, as is the critical Rayleigh number (Ra_{ec}) range discovered from the simulations; both are within the same order of magnitude.

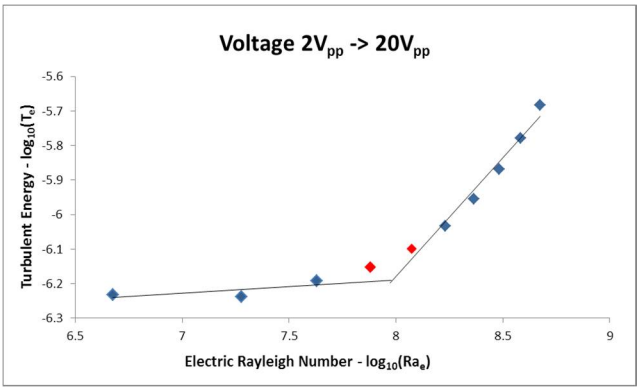

Figure 9. T_e vs Ra_e (from simulated data).

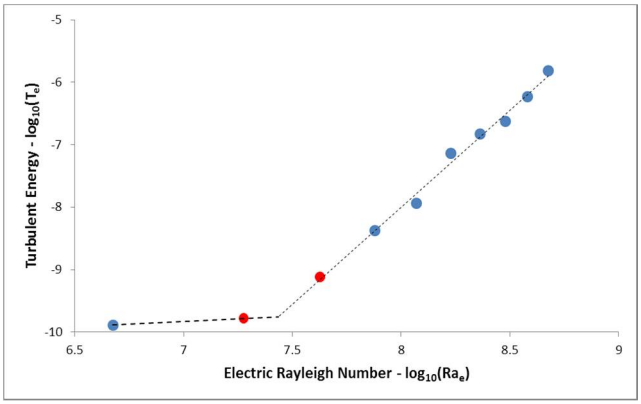

Figure 10. T_e vs Ra_e (from experimental data).

Preprints (www.preprints.org) | NOT PEER-REVIEWED | Posted: 19 November 2018 doi:10.20944/preprints201811.0462.v1

Table 1. T_e vs Ra_e Results

	Ra_{ec} (range)	log-log Laminar Slope	log-log Turbulent Slope	Turbulent Slope/ Laminar Slope
Simulation Results	1.18e7 - 7.57e7	0.044	0.690	15.738
Wang Results	1.9e7 - 4.3e7	0.16	3.03	18.938

3.3 Three Dimensional Flow

With inhomogeneous, 3D flow being a basic feature of turbulence [2], evidence can be found visually by looking to Figure 5 and Figure 11 or, more analytically, by referring to Figure 12 which shows a distribution of T_e along z similar to the Wang et al. results. It must be noted that the Wang results show unforced values of T_e on the order of 10^{-10} and mean *forced* values of 10^{-7} while this thesis reports values of $10^{-7}$and 10^{-6}, respectively.

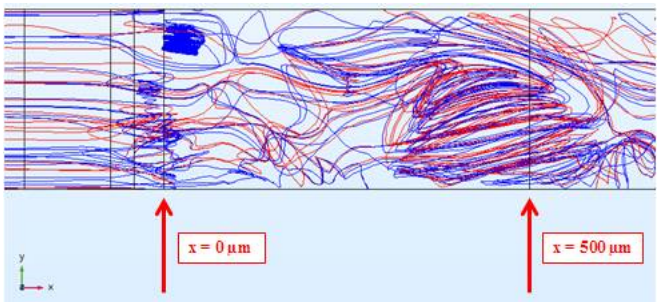

Figure 11. Transverse view 3D velocity streamlines in channel entrance.

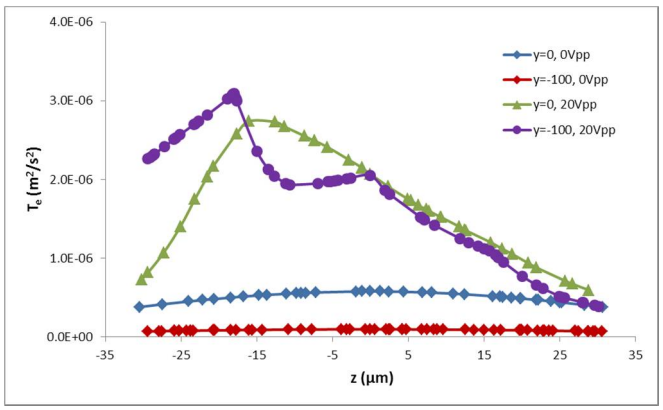

Figure 12. T_e vs z (inhomogeneity of flow in transverse plane)

For a voltage of $20V_{pp}$, the experimental data showed that at $z = 0$ µm in the y-direction, the value for T_e at y = 0 µm was about 2.7 times larger than the value at y = -100 µm (see Figure 13) which is understandable as the value of T_e is greater towards the centerline of the channel as depicted in Figure 12. The simulation results showed a maximum difference of 1.4 times at z = -15 µm.

Preprints (www.preprints.org) | NOT PEER-REVIEWED | Posted: 19 November 2018 doi:10.20944/preprints201811.0462.v1

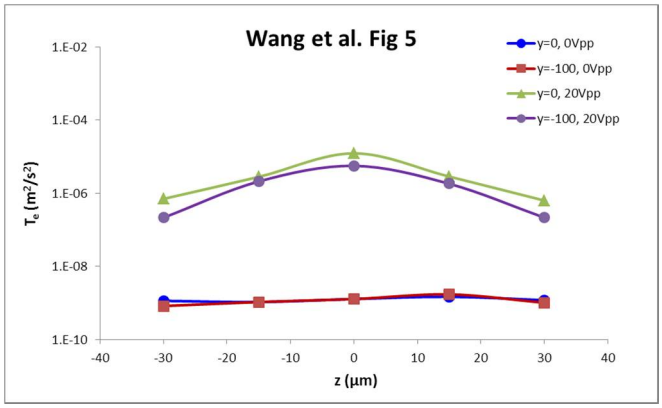

Figure 13. T_e vs z (Wang et al. experimental data).

3.4 Irregularity

The irregularity feature of turbulence is plotted as a time trace of the velocity at point (100, 0, 0). While fluctuations in the value of u_s became greater as the voltage increased in the experimental paper, the results of this work showed relatively constant values over time, Figure 14. However, the mean experimental values are on the same order as those found in these simulations; see Table 2 for a comparison of the experimental-to-thesis values (dashed lines are experimental values.

Table 2. Mean u_s value comparisons.

	u_s at $0V_{pp}$	**u_s at $8V_{pp}$**	**u_s at $20V_{pp}$**
Simulation Results	3.96	4.37	7.50
Wang Results over (0.25s)	3.23	4.65	11.29

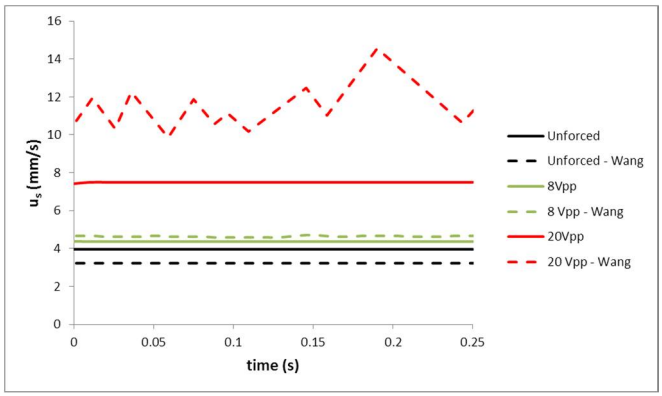

Figure 14. u_s vs time.

3.5 Entropy

The entropy calculated by the simulations in this work come from two sources, the flow itself and the transport of the NaCl ions using Equation 6. **Error! Reference source not found.** shows the values for each component of the entropy calculated at time t = 0.25s.

Error! Reference source not found. shows the entropy generated by the forced flow and Figure 16 shows the entropy generated by the species transport, both at three different forcing voltages. While the transport component contributes the majority of entropy to the system initially (on the order of 10^{-9} compared to 10^{-11}), its contributions diminish over time as the concentration gradient

Preprints (www.preprints.org) | NOT PEER-REVIEWED | Posted: 19 November 2018 doi:10.20944/preprints201811.0462.v1

decreases from 5000:1 towards equilibrium at which point the contributions are separated by only a single order of magnitude.

Table 3. Entropy components (at t = 0.25s).

	S_{gen} at $0V_{pp}$	S_{gen} at $8V_{pp}$	S_{gen} at $20V_{pp}$
Entropy$_{flow}$	1.65E-13	9.17E-13	2.70E-11
Entropy$_{TDS}$	2.89E-10	5.27E-10	6.04E-10
Entropy$_{total}$	2.90E-10	5.28E-10	6.31E-10

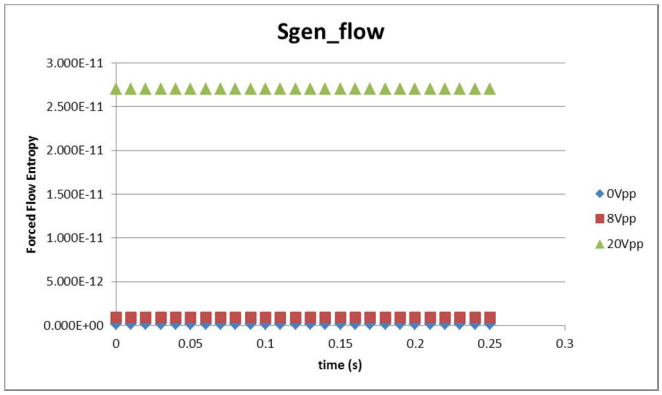

Figure 15. Entropy generated by flow.

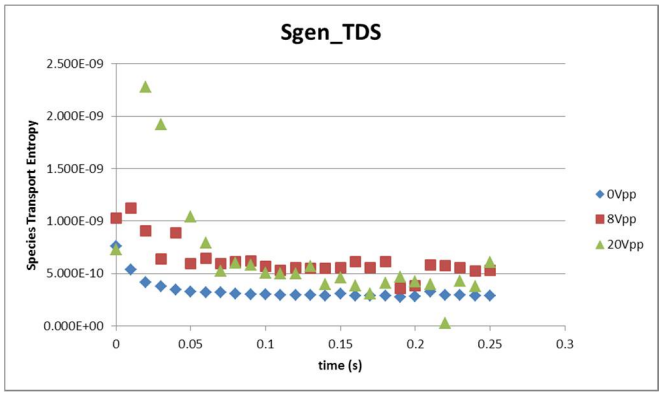

Figure 16. Entropy generated by species transport.

Alternatively, the entropy generated by the flow has a smaller magnitude but is constant over the length of the simulation and it illustrates the impact that the increase in forcing voltage has on the flow entropy. The increase from $0V_{pp}$ to $8V_{pp}$ is less than 1 order of magnitude while the increase from $8V_{pp}$ to $20V_{pp}$ increases the entropy value by 2 orders of magnitude.

4. Conclusions

The results of this work show that it is possible to observe the turbulent flow properties witnessed in the electrokinetically-forced microfluidic mixer experiments performed by Wang et al. [2] using CFD simulations. While the calculated values for the quantities of interest were not the same as the experimental data, the values were within the same order of magnitude of those reported by the experiments and showed the same trends in each of the indicators of turbulence looked at: fast diffusion, high dissipation, irregularity and 3-D flow.

The results section illustrates the effects of electrokinetic forcing in microfluidic mixing found through the use of CFD software. Figure 7 & Figure 8 depict the fast diffusion in the channel that

Preprints (www.preprints.org) | NOT PEER-REVIEWED | Posted: 19 November 2018 doi:10.20944/preprints201811.0462.v1

takes place within 0.25s of starting the flow and applying the electric field. The concentration has reached a near-homogeneous state at x = 0.5mm and secondary flows have started downstream which shows that a 5.0 mm channel is more than long enough for complete mixing of the 2 fluids; in fact a 0.75mm channel would likely suffice to completely mix the fluids in 0.25s. From Figure 12 it can be seen that with a $20V_{pp}$ forcing voltage the turbulent energy increases by up to two orders of magnitude (10^8 - 10^6) which indicates a greater mixing capability and, by extension, greater heat transfer potential; the two-magnitude increase in entropy seen in figures **Error! Reference source not found.** - Figure 16 would indicate the same.

Discrepancies in the range of T_e compared to Wang et al. may be due to assuming-out real world phenomena in an effort to simplify the simulations. Adding in the effects from an electroosmotic-wall boundary condition and the drag effects on the fluid due to the movement of the sodium and chlorine atoms in the electric field may help to explain the differences seen between the experimental and simulation data. Also, this study was done using laminar flow equations that are much less complex than the turbulent model equations. While there are many different turbulence models that can be used for incompressible turbulent flow, the standard is the Reynolds averaged Navier-Stokes (RANS), κ-ε model [9].

The RANS equation showing the components of turbulent kinetic energy (k here) [10] using the Einstein summation notation is shown in Equation 13

$$\underbrace{\frac{\partial k}{\partial t}}_{\text{Local derivative}} + \underbrace{\bar{u}_j \frac{\partial k}{\partial x_j}}_{\text{Advection}} = \underbrace{\frac{1}{\rho_0}\frac{\partial \overline{u_i' p'}}{\partial x_i}}_{\text{Pressure diffusion}} - \underbrace{\frac{1}{2}\overline{k u_j' u_j' u_i'}}_{\substack{\text{Turbulent transport} \\ \mathcal{T}}} + \underbrace{\frac{1}{\mu}\frac{\partial^2 k}{\partial x_j^2}}_{\substack{\text{Molecular viscous transport}}} - \underbrace{\overline{u_i' u_j'}\frac{\partial \bar{u}_i}{\partial x_j}}_{\substack{\text{Production} \\ \mathcal{P}}} - \underbrace{\frac{1}{\mu}\overline{\frac{\partial u_i'}{\partial x_j}\frac{\partial u_i'}{\partial x_j}}}_{\substack{\text{Dissipation} \\ \varepsilon_k}} - \underbrace{\frac{g}{\rho_0}\overline{\rho' u_i'}\delta_{i_3}}_{\substack{\text{Buoyancy flux} \\ b}} \qquad (13)$$

The five right-most terms in Equation 13 are not accounted for in this thesis and may account for deviations from the experimentally observed data.

Future research:

- Move the trailing edge of the inlet dividing plate to the entrance of the channel instead of upstream. This may eliminate secondary flows that occur before the fluid enters the channel and confine the entropy generation to the channel (i.e. largest Δσ is at the plane x = 0).
- Run simulations at the *Normal* mesh resolution and increase the solution time to determine the time needed to reach a fully-mixed outflow.
- Incorporate heat transfer into the simulation to quantify the effects of μEKT on heat transfer.
- Develop simulations using the COMSOL *Turbulent Flow* interface for comparison to the results presented here and to provide additional validation for Wang et al. experiments.

5. Nomenclature

C, c	concentration, mol/m³
D_e	Diffusion coefficient
D_{eff}	effective diameter, m
R	Rydberg gas constant, 8.314 J/K·mol
$\vec{F}_d$	drag force, N
$\vec{F}_e$	electrokinetic body force, N
$\vec{E}$, Eo	electric field, V/m
$\vec{v}$	velocity field (u, v, w), m/s
k	thermal conductivity, W/m·K
k	turbulent kinetic energy (Conclusions)
S_{gen}	entropy generation rate, W/ m³·K
T_e	turbulent kinetic energy, m²/s²
P, p	pressure, Pa
Δp	pressure drop, Pa
D_e	diffusivity (or diffusion coefficient 1.5 x 10-9 m²/s)

 doi:10.20944/preprints201811.0462.v1

ε	absolute permittivity
ε_o	vacuum permittivity, 8.854×10^{-12} F/m
ε_r	relative permittivity
ϱ	fluid density, kg/m^3
ϱ_v	charge density, C/m^2
ϱ_f	free charge density, C/m^2
σ_1	conductivity of distilled water
σ_2	conductivity of NaCl solution
μ	dynamic viscosity, kg/m·s
ω	channel width at entrance, m

Author Contributions: Conceptualization, W.L.D. and E.C.L.; methodology, W.L.D. and E.C.L.; validation, W.L.D.; formal analysis, W.L.D.; writing—original draft preparation, W.L.D.; writing—review and editing, W.L.D. and E.C.L.; visualization, W.L.D.; supervision, E.C.L.; funding acquisition, E.C.L.".

Funding: This work was partially sponsored by the National Science Foundation grant ACI-1429702 (funding for UCO's Buddy Supercomputing Cluster).

Acknowledgments: The authors would like to acknowledge Dr. Guiren Wang from the University of South Carolina and his team for providing both the inspiration for this study as well as his expertise. Also the Dept. of Engineering & Physics at the University of Central Oklahoma for their support.

References

1. Chen, Chuan-Hua, et al. "Convective and absolute electrokinetic instability with conductivity gradients." Journal of Fluid Mechanics 524 (2005): 263-303.
2. Wang, G. R., Fang Yang, and Wei Zhao. "There can be turbulence in microfluidics at low Reynolds number." Lab on a Chip 14.8 (2014): 1452-1458.
3. Ahmed, Daniel, et al. "A fast microfluidic mixer based on acoustically driven, sidewall-trapped microbubbles." Microfluidics and Nanofluidics 7.5 (2009): 727-731.
4. Storey, Brian D., et al. "Electrokinetic instabilities in thin microchannels." Physics of Fluids (1994-present) 17.1 (2005): 018103. aip.scitation.org/doi/10.1063/1.1823911
5. Baygents, J.C. and F. Baldessari, "Electrohydrodynamic instability in a thin fluid layer with an electrical conductivity gradient". Physics of Fluids 10 (1998): 301.
6. Wang, G. R., Fang Yang, and Wei Zhao. "Microelectrokinetic turbulence in microfluidics at low Reynolds number." Physical Review E 93.1 (2016):013106-1 - 013106-9. dx.doi.org/10.1103/PhysRevE.93.013106.
7. Wang, Guiren. Email correspondence with author, December 2016.
8. Herwig, Heinz. "What Exactly is the Nusselt Number in Convective Heat Transfer Problems and are There Alternatives?" Entropy 18.5 (2016): 198.
9. Ngoc-cuong Nguyen. "Turbulence Modeling". MIT, 5 Nov. 2005. Web. 26 Dec. 2016. www.mit.edu/~cuongng/Site/Publication_files/TurbulenceModeling_04NOV05.pdf
10. "Turbulence kinetic energy." Wikipedia. Wikimedia Foundation, n.d. Web. 06 Jan. 2017. en.wikipedia.org/wiki/Turbulence_kinetic_energy.